APPLIED SCIENCES AND ENGINEERING

Amphiphilic hemicyanine molecular probes crossing the blood-brain barrier for intracranial optical imaging of glioblastoma

Wei Qin[1,2]*†, Honghui Li[1,2]†, Jiali Chen[1,3]†, Yang Qiu[1], Limin Ma[1], Liming Nie[1,2]*

Intracranial optical imaging of glioblastoma (GBM) is challenging due to the scarcity of effective probes with blood-brain barrier (BBB) permeability and sufficient imaging depth. Herein, we describe a rational strategy for designing optical probes crossing the BBB based on an electron donor-π-acceptor system to adjust the lipid/water partition coefficient and molecular weight of probes. The amphiphilic hemicyanine dye (namely, IVTPO), which exhibits remarkable optical properties and effective BBB permeability, is chosen as an efficient fluorescence/photoacoustic probe for in vivo real-time imaging of orthotopic GBM with high resolution through the intact skull. Abnormal leakage of IVTPO adjacent to the developing tumor is unambiguously observed at an early stage of tumor development prior to impairment of BBB integrity, as assessed by commercial Evans blue (EB). Compared with EB, IVTPO demonstrates enhanced optical imaging capability and improved tumor-targeting efficacy. These results offer encouraging insights into medical diagnosis of intracranial GBM.

INTRODUCTION

Glioblastoma (GBM) is one of the most common malignant tumors of the central nervous system (CNS), and this fast-growing, aggressive tumor has a poor prognosis and high mortality (*1*–*3*). For an early diagnosis and successful treatment of GBM, unambiguous visualization of its pathological features and a clear understanding of its molecular pathogenesis are required (*4*, *5*). To achieve these, utilization of brain-imaging modalities and the development of corresponding contrast agents are of great importance.

The current clinical modalities for brain imaging, including computed tomography (CT), positron emission tomography (PET), single-photon emission computed tomography (SPECT), and magnetic resonance imaging (MRI), all greatly rely on expensive and bulky modern instruments (*6*). Although these imaging techniques generally exhibit high penetration depth, they also suffer characteristic shortcomings, including hazardous ionizing radiation (CT, PET, and SPECT), poor contrast (CT), and limited spatial resolution (MRI and PET) (*6*–*8*). Clinical applications of these techniques are somewhat restricted by these shortcomings. In comparison, optical imaging has none of the abovementioned shortcomings. Moreover, optical imaging has distinct advantages, including high sensitivity, high resolution, nonionizing radiation, and real-time and in situ monitoring capabilities (*9*). Common commercial dyes, including rhodamine, cyanine, and Evans blue (EB), are now in wide use in biological research (*10*–*12*). Although they exhibit remarkable optical imaging performance and promising application prospects for medical diagnosis (*13*), they are rarely applied as effective BBB-crossing probes for optical imaging owing to their large molecular weight (MW) and unsuitable lipophilicity (*14*). Overall, two major hurdles to intracranial optical imaging of GBM still remain: (i) the absence of an effective BBB-crossing optical probe or contrast agent and (ii) its comparatively poor imaging penetration depth (*15*).

The blood-brain barrier (BBB) is a semipermeable barrier encompassing the microvasculature of the CNS, and this functions to preserve the CNS from exposure to toxins and pathogens in blood (*16*–*18*). Because of its protective function, the BBB impedes the passage of most molecular probes and more than 98% of small-molecule drugs into the brain (*19*, *20*). This is a major problem for drug delivery and for optical imaging using probes. To mitigate this problem, various nanotechnology-based methods have been developed to deliver probes or therapeutics across the BBB (*20*–*27*). However, several issues still hamper their widespread applications, including the reliance on multicomponent systems with complicated mechanisms, low loading content, premature release, and potential adverse effects (*21*).

A simple yet effective method to circumvent these problems is to specifically design small-molecule optical probes for intracranial GBM imaging that are capable of crossing the BBB. For this, these small-molecule probes are expected to demonstrate favorable molecular characteristics, high reproducibility, and biocompatibility. The crucial factors that must be taken into consideration include absorption and emission wavelength, signal strength, MW, and lipophilicity (*14*, *28*, *29*). Optical imaging using designed probes should afford clear visualization and effective monitoring of the heterogeneous microstructure of vasculature (*30*), the abnormal efflux of molecules (*31*), and other pathological features in tumor progression. Hence, through the development of imaging probes with BBB permeability, it should be possible to satisfy the urgent needs for fundamental research in GBM and a clear clinical diagnosis.

Fluorescence (FL) imaging is a powerful biomedical imaging modality, and it is capable of providing abundant information of physiological and pathological importance at the cellular and tissue levels (*9*, *32*, *33*). For the generation of high-resolution images at the desired depth, common craniotomy is generally required for brain imaging (*34*, *35*). However, these invasive and destructive operations are far from ideal. They are known to impair BBB integrity, which becomes susceptible to hemorrhage, infection, and inflammation, leading to compromised imaging quality and a high mortality

[1]Medical Research Institute, Guangdong Provincial People's Hospital (Guangdong Academy of Medical Sciences), Southern Medical University, Guangzhou 510080, China. [2]Guangdong Cardiovascular Institute, Guangzhou 510080, China. [3]School of Medicine, South China University of Technology, Guangzhou 510006, China.
*Corresponding author. Email: qinwei@gdph.org.cn (W.Q.); nieliming@gdph.org.cn (L.N.)
†These authors contributed equally to this work.

rate in animals (*36*, *37*). Photoacoustic imaging, an emerging modality that elegantly fuses the distinctive capabilities of light and sound, breaks the fundamental penetration depth barrier of traditional optical imaging, enabling high-resolution images with a greatly improved penetration depth of up to several centimeters (*38*–*40*). Compared to conventional single-photon FL imaging, photoacoustic imaging provides superior resolution for the sensitive detection of brain tumors at the micrometer scale. Moreover, it enables the utilization of abundant optical endogenous contrasts to offer in vivo structural and functional information. The bimodal FL/photoacoustic imaging modality combines the intrinsic advantages of both techniques, potentially alleviating the problem of insufficient penetration depth to acquire more information about the biological microenvironment of deep tissues (*41*–*44*).

With these frontier issues in our minds, a rational strategy for the design of optical probes that efficiently cross the BBB is developed (Fig. 1). Molecular fusion of a strong electron donor-acceptor (D-A) system linked with a π bridge favors the intramolecular charge transfer (ICT) from an electron-donating unit to an electron-accepting moiety, leading to a strong absorption and red-shifted emission (*45*). Structural modulation toward the lipid/water partition coefficient (log *P*) and MW of the probes is to reduce the MW and adjust lipophilicity to enhance BBB permeability. The probe chosen for further study, abbreviated as IVTPO, exhibits a unique amphiphilic property, strong optical absorption, distinct near-infrared (NIR) emission, and outstanding BBB penetration. This efficient optical probe is subsequently assessed by in vivo real-time imaging of intracranial GBM through the intact skull. Using this probe, visualization of the microscopic pathological features of GBM progression at high resolution is achieved (Fig. 1).

RESULTS

Design, synthesis, and optical properties of probes

Hemicyanine dyes (*46*) abbreviated as IVPM, IVTM, and IVTPO (Fig. 2A) were designed with the same electron-accepting group (an indolium ion) but different electron-donating moieties (aromatic amine and/or thiophene units). Molecular linkage of a strong electron D-A structure together with a π bridge favors formation of a dye with intense optical absorption and distinct NIR emission (*47*–*50*), which is particularly beneficial for high-contrast optical imaging. These hydrophilic positively and negatively charged functional groups are attached to a hydrophobic organic backbone to generate amphiphilic molecular structures. The synthetic routes for preparation of

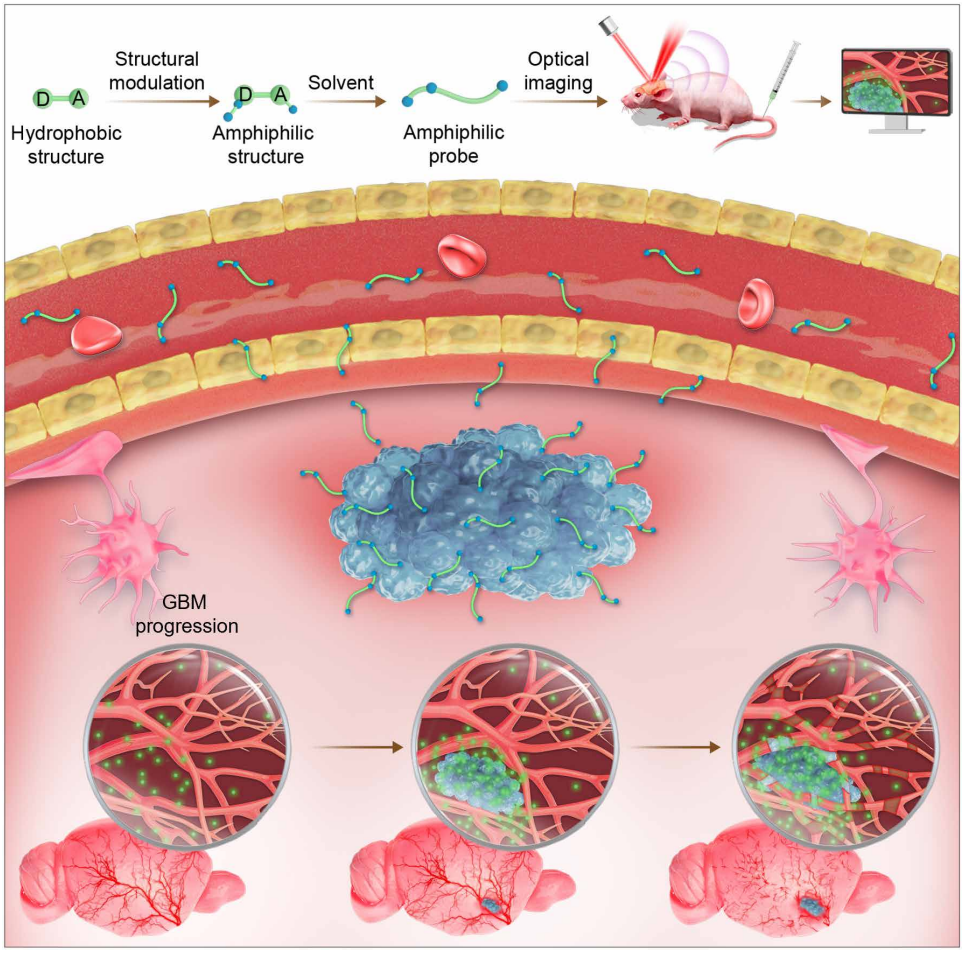

Fig. 1. Rational design of BBB permeability probes for optical imaging of GBM. Rational design of amphiphilic hemicyanine molecular probes crossing the BBB for intracranial optical imaging of GBM.

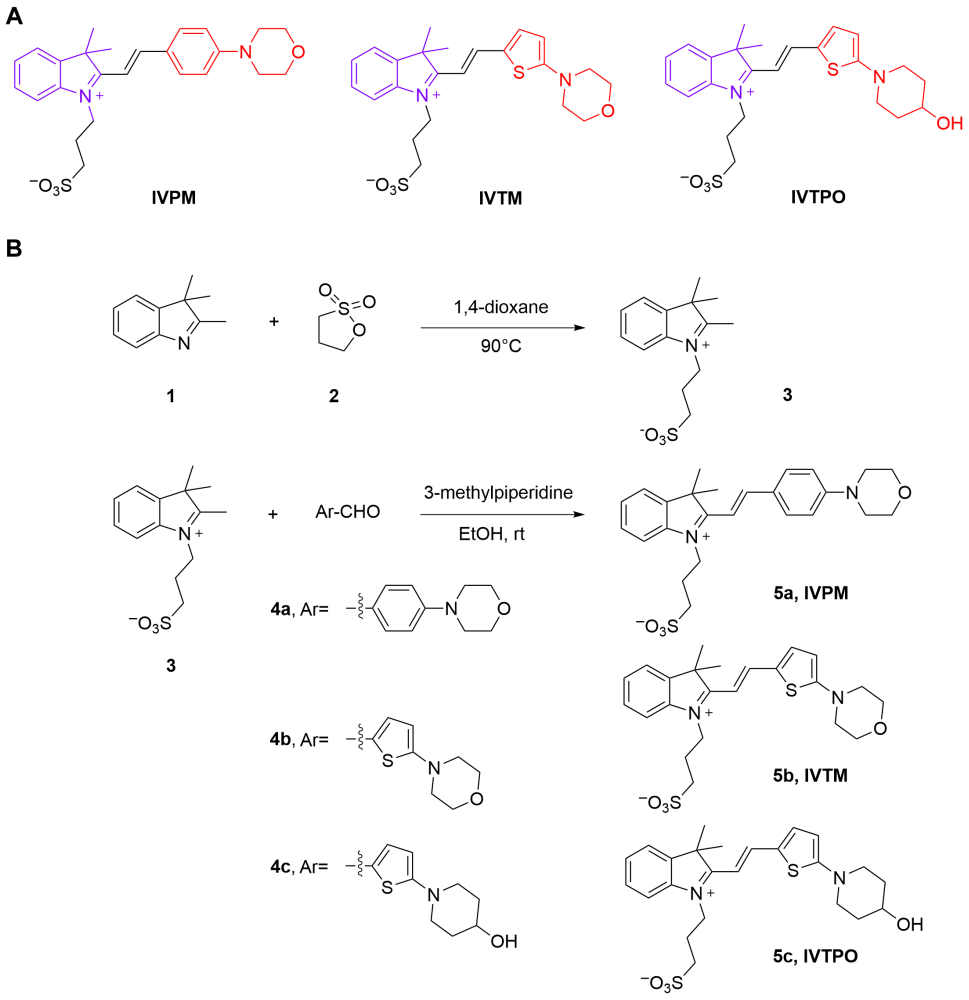

Fig. 2. Chemical structures and synthesis of the optical probes. (**A**) Chemical structures and (**B**) synthetic routes to IVPM, IVTM, and IVTPO. rt, room temperature.

these probes are shown in Fig. 2B. The hydrophilic intermediate 2,3,3-trimethyl-1-(propan-3-sulfonyl)indolenine was facilely synthesized in 1,4-dioxane at an elevated temperature. A subsequent Knoevenagel condensation using ethanol as the organic solvent and 3-methylpiperidine as a basic catalyst proceeded smoothly at room temperature, yielding the final compounds with satisfactory yields (>60%). In contrast with previous synthetic methods (*51*–*54*), the method reported here is mild, facile, and suitable for various aromatic aldehydes with different substituents. Moreover, it skillfully circumvents the use of controlled chemicals or reagents as a catalyst (e.g., acetic anhydride and piperidine).

The chemical structures of the products were subsequently characterized by standard spectroscopic techniques and ultrahigh-performance liquid chromatography–tandem mass spectrometry. The results confirmed that the chemical structures were correct and that the samples were of high purity (see figs. S1 to S15 in the Supplementary Materials). The coupling constants for vinyl protons of the hemicyanine dyes in the proton nuclear magnetic resonance (NMR) spectra are all above 12 Hz, revealing that they have typical trans conformations. Formation of the trans isomers is favored in the Knoevenagel reaction at room temperature because the trans conformations are thermodynamically stable, whereas steric hindrance hampers formation of the cis configurations. The absence of NMR peaks for the minor cis isomers is probably because they were removed during the product purification process.

IVPM, IVTM, and IVTPO are all soluble in common organic solvents such as dichloromethane (DCM), methanol, and dimethyl sulfoxide (DMSO). The absorption spectra of IVPM, IVTM, and IVTPO in DMSO are peaked at 531, 572, and 572 nm, respectively (Fig. 3A). Corresponding optical energy gaps estimated from onset of the absorption spectra are 2.07, 2.05, and 2.05 eV, respectively (Table 1). Molar absorption coefficients (ε) of IVPM, IVTM, and IVTPO in DMSO are calculated as 5.34×10^4, 10.94×10^4, and $12.29 \times 10^4\ M^{-1}\ cm^{-1}$, respectively (Table 1). Their emission maxima in DMSO are located at 625 to 635 nm, with emission tails extending to the NIR region at 800 nm (Fig. 3A). Unlike traditional commercial dyes with small Stokes shifts (generally <25 nm) (*55*), they have sufficient Stokes shifts with a negligible overlap between absorption and emission spectra. Together, the absorption spectra, emission spectra, and molar absorption coefficient data reveal the strength of the electron D-A systems (IVTPO > IVTM > IVPM). To enhance comprehension of the impact of various electron-donating groups (D_1, D_2, and D_3) on optical property, we assessed the vertical ionization energy (VIE) through density functional

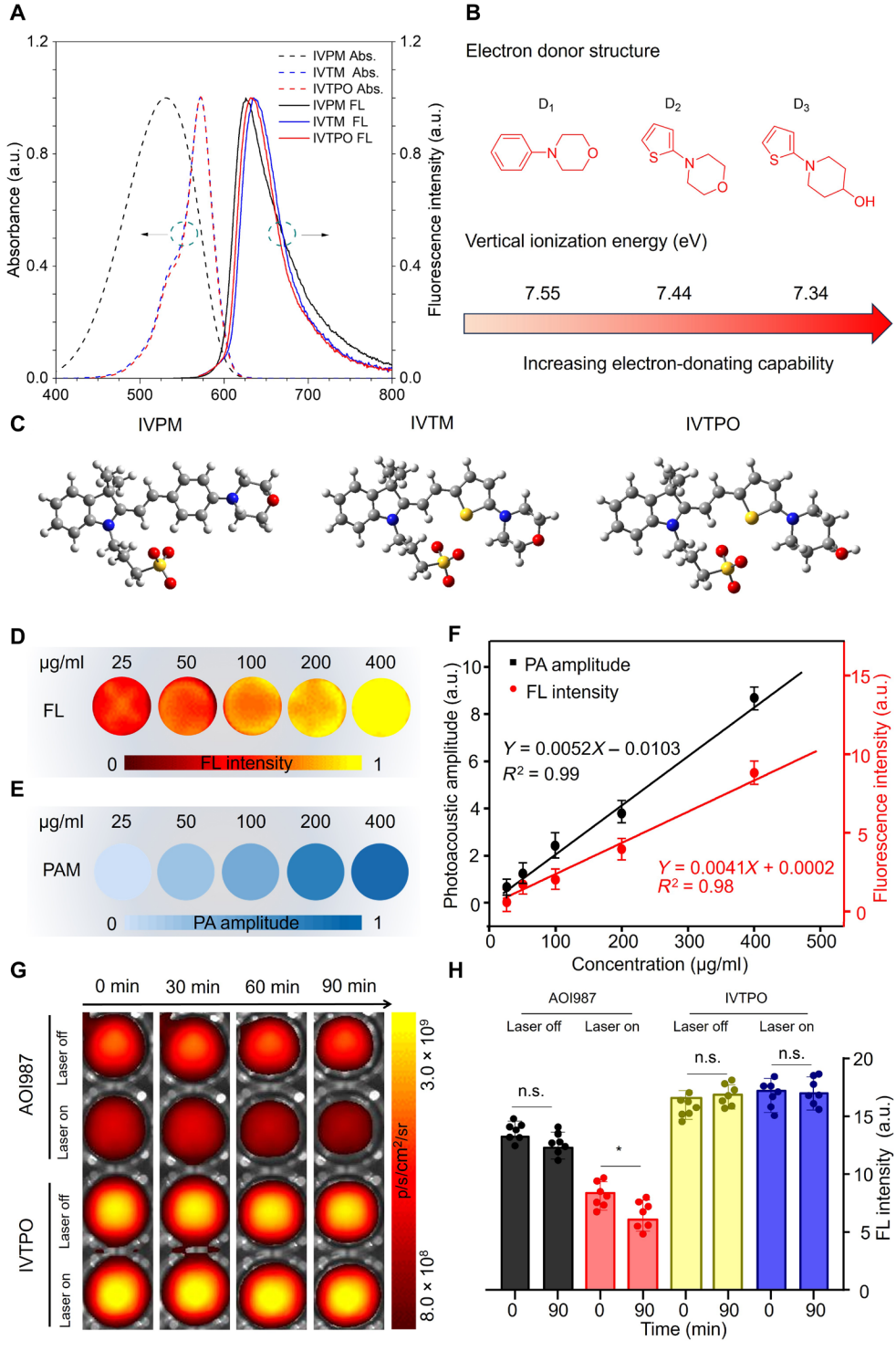

Fig. 3. Optical properties of probes. (**A**) Normalized absorption and FL spectra of IVPM, IVTM, and IVTPO. a.u., arbitrary units. (**B**) Vertical ionization energies of different electron-donating groups of IVPM, IVTM, and IVTPO. (**C**) Optimized molecular geometries of IVPM, IVTM, and IVTPO. (**D**) FL images of IVTPO in an aqueous solution at various concentrations (25 to 400 μg/ml). (**E**) Photoacoustic (PA) images of IVTPO in an aqueous solution at various concentrations (25 to 400 μg/ml). (**F**) Relationship between FL/photoacoustic intensity and probe concentration (25 to 400 μg/ml). (**G**) FL images of photostability of AOI987 and IVTPO at various time points. (**H**) Quantitative results of FL intensities and designed time points in (G). n.s., not significant.

Table 1. Molecular properties of IVPM, IVTM and IVTPO.

	MW (Da)*	log $P^{\dagger}$	λ_{ab} (nm)‡	ε (M^{-1} cm^{-1})§	λ_{em} (nm)¶	FWHM (nm)$^{\#}$	Stokes shift (nm)**	E_g (eV)††	VIE (eV)‡‡
IVPM	455	0.76	531	5.34×10^4	626	62	95	2.07	7.55
IVTM	461	0.39	572	10.94×10^4	635	53	63	2.05	7.44
IVTPO	475	0.41	572	12.29×10^4	635	52	63	2.05	7.34

*MW is the molecular weight. †log *P* is the lipid/water partition coefficient measured by a shake flask experiment. ‡λ_{ab} is the absorption maximum in DMSO. §ε is the molar absorption coefficient in DMSO. ¶λ_{em} is the emission maximum in a DMSO solution. #FWHM is the full width at half maximum in DMSO. **Stokes shift is the difference between the wavelengths of absorption and emission of a molecule. ††E_g is the optical energy gap estimated from the onset of the absorption spectrum in DMSO. ‡‡VIE is the vertical ionization energy obtained from DFT calculations.

theory (DFT) calculations. As shown in Fig. 3B, the VIEs of D_1, D_2, and D_3 are calculated to be 7.55, 7.44, and 7.34 eV, respectively. Hence, the electron-donating strength follows the order $D_3 > D_2 > D_1$. The stronger electron-donating strength contributes to an improved electron push-pull effect, generating enhanced absorption and red-shifted emission. To gain insights into their molecular structures and optical properties, we conducted DFT calculations at the molecular level. As depicted in Fig. 3C, the torsion angles in IVPM, IVTM, and IVTPO between the central double bond and the adjacent phenyl ring or thiophene unit are 1.2°, 1.8°, and 2.5°, respectively. Similarly, the torsion angles between the central double bond and the adjacent indolium ring are 1.1°, 2.2°, and 1.0°, respectively. The results suggest relatively planar molecular conformations with good conjugation and π-electron delocalization. These calculated results show agreement with the aforementioned experimental results (summarized in Table 1).

Different from most hydrophobic hemicyanine dyes of high MW, the three probe molecules are amphiphilic and of low MW (<500 Da). The oil-water partition coefficient (log *P*) is an essential indicator to evaluate the potential for BBB penetrability (*56*). To measure the log *P* for these probes, we performed a shake flask experiment. The log *P* value of IVTPO was determined to be 0.41, which is higher than that of commercial Thioflavin T (ThT) (0.16) (*56*). Thus, these results suggest that IVTPO exhibits higher lipophilicity and better BBB penetrating potential compared with ThT. The high molar absorptivity, remarkable NIR emission, good solubility, and satisfactory BBB penetrating potential of IVTPO encourage us to further examine its optical properties and potential bioimaging applications.

As a first step to facilitate imaging applications of IVTPO in a biological environment, the optical properties of IVTPO in an aqueous solution were assessed. As shown in Fig. 3 (D to F), the FL and photoacoustic intensity of an IVTPO aqueous solution increases linearly at low concentrations (25 to 400 μg/ml). Because sufficient photostability is indispensable for long-term optical imaging, loss of IVTPO FL was compared with loss of AOI987 (*57*) FL (a commercial dye) in the absence and presence of continuous laser excitation (Fig. 3G). In the absence of laser excitation, only a slight decrease in the FL intensity of AOI987 could be detected. However, under continuous laser irradiation (stable excitation with 1 mW for 90 min) at 532 and 559 nm, a marked decrease in AOI987 FL intensity was observed (Fig. 3H), with FL intensity in the control group decreasing from 8.25 to 5.75 (a 30% drop). In comparison, no pronounced decrease in the FL intensity of an aqueous solution of IVTPO was observed under the same experimental conditions (Fig. 3H). Hence, IVTPO exhibits good photostability and is suitable for long-term optical imaging.

BBB permeability study of the optical probe and in vitro FL imaging

An in vitro BBB model prepared by seeding bEnd.3 cells onto the gelatin-coated upper chamber of a Transwell plate was used to confirm the BBB permeability of IVTPO (Fig. 4A) (*58*). This system comprises a well plate with a semipermeable membrane that separates each well in two compartments, representing the apical side (blood side) and the basolateral side (brain side) of the BBB (*59*). EB and AOI987 (*57*) were used in the experiment as a negative and a positive control, respectively. Minimal FL of the dispersed EB dye was observed in the lower chamber even after 120 min. In comparison, IVTPO yielded different experimental results. After 30 min, a diffused IVTPO dye color could be observed in the lower chamber by the naked eye (Fig. 4B). As the incubation time increased, the color became darker, indicating that more dye molecules were migrating through the micropores of the membranes and dispersing into the lower chamber. Quantitative analysis of the results is consistent with the experimental phenomenon. IVTPO exhibits a satisfactory transcellular diffusion efficiency (27%), which is comparable to that of the positive control AOI987 (26%) but much higher than that of the negative control EB (2%) (Fig. 4C). Prompted by the ability of IVTPO to cross BBB monolayers in vitro, we next examined its ability to permeate the BBB in vivo using intravital real-time confocal laser scanning microscopy on healthy mice (fig. S16). At 10 and 30 min after an intravenous injection, intense FL from IVTPO was observed in the mouse brain. Conversely, FL was minimal in the mouse brain at 30 min after intravenous injection of EB. After sufficient cardiovascular perfusion, the mouse brain was extracted for ex vivo imaging. Intense FL was observed in the mouse brains harvested from the IVTPO group, indicating the presence of the optical dye in the brain parenchyma rather than only in brain vessels (fig. S16). This favorable outcome was indicative of rapid penetration of IVTPO through an intact BBB.

To examine cellular uptake of IVTPO molecules, macrophage cells and U87-MG cells were chosen as model cell systems. Intense FL from probe molecules was observed in the cellular environment of both macrophage cells and U87-MG cells, revealing the typical cellular internalization by endocytosis (Fig. 4D). This remarkable capability of cellular uptake of probe molecules by these cells favors for GBM imaging in vivo. However, the FL signal in the cytoplasm could gradually disappear with extension of incubation time to 12 hours (Fig. 4E), possibly due to the metabolism of living cells in the cytoplasm. The cytotoxicity of IVTPO was evaluated by metabolic viability of macrophage cells and U87-MG cells, respectively, after incubation with different concentrations of dye (10 to 100 μg/ml).

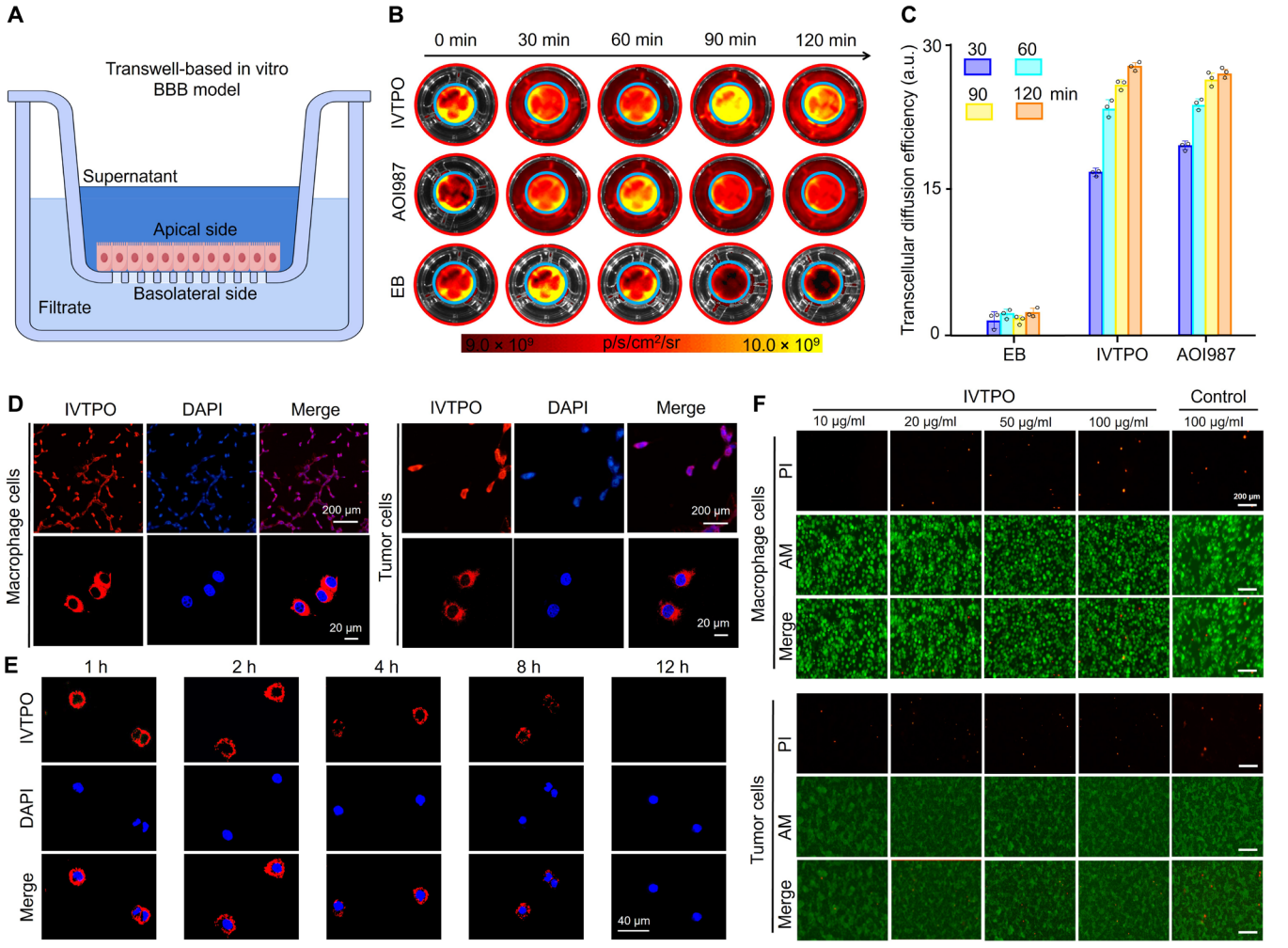

Fig. 4. BBB permeability study and cell imaging of the optical probe. (**A**) Schematic diagram of the in vitro BBB monolayer model. (**B**) FL images of IVTPO, AOI987, and EB of in vitro BBB monolayer model. (**C**) Quantitative results of transcellular diffusion efficiency in (B). (**D**) Confocal images of macrophage cells and U87-MG cells after incubation with IVTPO (100 μg/ml) for 2 hours at 37°C. DAPI, 4′,6-diamidino-2-phenylindole. (**E**) Confocal images of tumor cells on designated time points after incubation with IVTPO (100 μg/ml). h, hours. (**F**) Cytotoxicity of different concentrations of IVTPO (10 to 100 μg/ml) to macrophage cells and U87-MG cells.

As illustrated in Fig. 4F, even after incubation at the dye concentration of 100 μg/ml for 24 hours, the red FL from propidium iodide (PI) molecules was hardly observed, which is indicative of few dead cells. Thus, IVTPO exhibits negligible cytotoxicity under the experimental condition. To examine the biological safety of the optical probe in vivo, we subjected tissue sections of major organs (e.g., heart, liver, spleen, lung, kidneys, and brain) to hematoxylin and eosin (H&E) staining. No edema, hyperemia, inflammation, and/or any other notable abnormalities on organs were detected after continuous intravenous injection of IVTPO for 30 days, indicating negligible toxicity of the probe to organs under the experimental condition (fig. S17).

In vivo photoacoustic imaging of GBM through the intact skull and biodistribution study

A GBM-bearing mouse model was established by intracerebral administration of mCherry-labeled U87-MG cells. After a period of injection (normally 7 to 13 days), intense red bioluminescence (BL) was detected in the mouse brain, indicating successful generation of a tumor-bearing mouse model. Subsequent administration of IVTPO initiated a substantial enhancement of FL in the mouse brain (Fig. 5A). The pattern of intense IVTPO FL matched with the location of the tumor as indicated by BL (Fig. 5B). To further validate the association between BL and FL, we overlaid the FL signal regions from Fig. 5 (A and B), confirming their alignment (Fig. 5C). In addition, we performed a quantitative analysis of pixel counts in the BL and FL regions, with the results presented in fig. S18. The colocalization and quantitative analyses reveal that the distribution of intense IVTPO FL correlates with the tumor location, as indicated by its BL. Next, tumor-bearing mice were euthanized and their major organs, including the brain, heart, liver, lung, spleen, and kidneys, were collected for ex vivo imaging (after cardiovascular perfusion). Ex vivo FL imaging of the organs suggests that (except the liver and kidneys) the optical probe molecules are specifically enriched in the brain tumor (Fig. 5B). This remarkable enrichment of optical probe molecules in the tumor is probably due to the

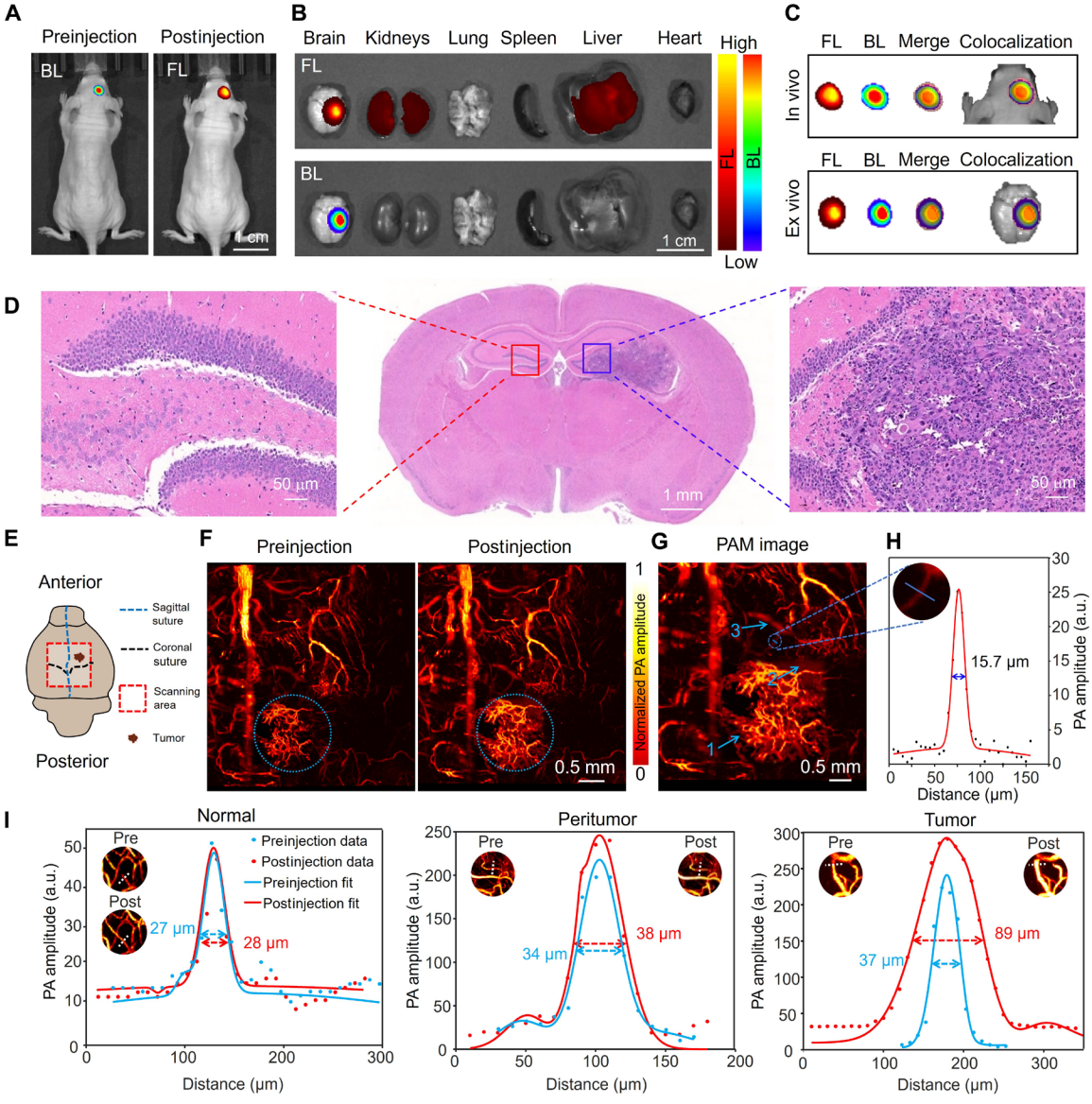

Fig. 5. Establishment of GBM-bearing mouse models and experimental results of photoacoustic imaging. (**A**) In vivo BL and FL images of GBM-bearing mice after the intravenous injection of IVTPO for 1 hour. (**B**) Ex vivo FL and BL images of major organs of GBM-bearing mice after the intravenous injection of IVTPO for 1 hour. (**C**) In vivo and ex vivo colocalization analyses of BL and FL images. (**D**) H&E staining of the brain tissue of a GBM-bearing mouse model. (**E**) Schematic diagram of the tumor position and skull structure of mouse model and imaging region of PAM. (**F**) Photoacoustic images of cerebral vessels of a GBM-bearing mouse before and after intravenous injection of IVTPO. (**G**) Representative photoacoustic image of cerebral vessels of a GBM-bearing mouse after intravenous injection of IVTPO for the illustration of tumor (1), dispersed probe (2), and cerebral cortical vessel (3). (**H**) Cross-sectional intensity profile measured along the blue line in (G). (**I**) Changes in blood vessel diameter in normal, peritumoral, and tumor regions before and after IVTPO injection.

enhanced permeability and retention effect (*60*) and the amphiphilic property of the probe. H&E staining analysis of brain sections further confirms the successful establishment of a GBM-bearing mouse model (Fig. 5D).

Compared with conventional FL imaging, photoacoustic imaging characteristically demonstrates superior penetration depth. Therefore, a preliminary photoacoustic microscopy (PAM) examination was performed to image orthotopic GBM on a tumor-bearing murine model through the intact skull (Fig. 5E). After intravenous administration of IVTPO, the probe promptly perfused in the blood vessels of the tumor, contributing to a substantial enhancement of photoacoustic signal in the tumor and surrounding regions (Fig. 5F). This outcome validates the efficacy of IVTPO for tumor imaging. To demonstrate the reproducibility of this experiment, we performed photoacoustic imaging on another tumor-bearing mouse under the same conditions. The complicated structure of cerebral cortical vessels, the exact position and morphology of the tumor, and the pronounced leakage of the optical probe could all be unambiguously visualized (Fig. 5G). Careful measurement of the PAM image enables quantitative analysis of the full width at half maximum of a tiny capillary (as indicated in the picture), which is calculated as 15.7 μm (Fig. 5H). Then, we conducted a comparative analysis of changes in blood vessel

diameter across the normal tissue, the peritumoral area, and the tumor region following IVTPO injection (Fig. 5I). The findings indicate a notable enlargement of vessel diameter within the tumor region after the injection, a modest increase in the peritumoral area, and no remarkable alteration in vessel diameter within the normal brain tissue. These observations indicate the effective tumor-targeting capability of IVTPO. Collectively, the results demonstrate that IVTPO serves as an efficient optical probe, facilitating noninvasive intracranial photoacoustic imaging of GBM to acquire extensive visual information at the microscopic level.

Encouraged by these positive results, we further used EB to assess the extent of BBB dysfunction during tumor progression (*61*, *62*). Initially, EB was administered to the tumor model mice to evaluate its accumulation within the tumor and to minimize the potential interference of residual dye with subsequent optical imaging (Fig. 6A). We calculated the mean photoacoustic intensity for both the region of interest (ROI) and the entire image. Our findings indicated that the photoacoustic intensity of EB in both regions generally returned to baseline levels 4 hours after injection and did not substantially interfere with the subsequent administration of IVTPO for optical imaging. Using this time point as a reference, we established a timeline for the experimental procedures outlined in this section (Fig. 6B) to systematically monitor pathological changes through the intact skull during the malignant progression of GBM. During the early stages of tumor development, when tumor morphology was hardly distinguishable, negligible extravasation of EB was observed (Fig. 6C). Because EB almost exclusively binds the macromolecule serum albumin in blood, it is essentially blocked by a relatively intact BBB. However, obvious diffuse signals from the IVTPO probe were observed adjacent to the cerebral vessels (indicated by white arrows). The indicated regions are probable sites of vulnerability in cerebral cortical vessels caused by tumor cells, although these microscopic sites do not permit notable leakage of EB. During the intermediate stages of GBM progression, typical tumor morphology was now distinguishable, although leakage of EB remained minimal. The precise tumor location, its characteristic morphology, and tumor angiogenesis could all clearly be monitored in the experimental group (Fig. 6D). A pronounced diffuse signal (indicated by white arrows) was observed in the peritumoral area, possibly indicating the existence of microscopically fragile cerebral vessels. Abnormal leakage of the optical probe in the peritumoral area was detected at the early and intermediate stages of tumor progression, prior to the impairment of BBB integrity (as evaluated by EB). This unique phenomenon could serve as an imaging indicator for the early detection of GBM. At advanced stages of GBM progression, the cerebrovascular structure of the tumor-bearing mouse shows a notable difference (Fig. 6E). Normal blood vessels of characteristic structure and morphology were only sparsely observed in each field of view, having been replaced by characteristic tumor blood vessels following the malignant growth of GBM. The disorganized structure and disordered distribution of these blood vessels could clearly be observed. This extensive damage to the BBB greatly promoted leakage of IVTPO into the bloodstream. Moreover, EB extravasation from tumor blood vessels could also be observed at this stage because of notable impairment of the BBB. These pathological changes can be observed in high-resolution images of the tumor tissue (Fig. 6F) and in vivid and real-time video footage (movie S1 in the Supplementary Materials). The white circles were used to annotate the ROIs corresponding to the BBB leakage areas, whereas the white arrows indicated the locations of the tumors. In addition, we quantified the changes in the average photoacoustic signal values both within the ROIs and the full images. The quantitative analyses of the photoacoustic images are presented in Fig. 6 (G to I). The error bars in the displayed curves represent the SD, calculated from independent measurements conducted on seven animals per group. Under identical conditions, IVTPO exhibits higher photoacoustic intensity than EB. Moreover, the application of IVTPO enables the real-time imaging of orthotopic GBM for 120 min. These results provide evidence that IVTPO is an efficient photoacoustic probe (and superior to EB under the same experimental conditions), enabling us to realize real-time monitoring of GBM progression with high resolution through the intact skull.

To explore the distribution profiles of IVTPO in various postinjection organs, analogous ex vivo FL examinations were performed on tumor model mice at early, intermediate, and advanced stages of the experiment. The corresponding quantification analyses are presented in Fig. 6 (J to L). The results demonstrate that IVTPO exhibits enhanced targeting efficacy toward brain tumors at various stages of tumor advancement. This is particularly notable during the initial stages when the BBB is still intact as IVTPO is able to penetrate the BBB effectively and accumulate predominantly within brain tumors. Overall, compared with commercial EB dye, the IVTPO probe demonstrates improved imaging capability and enhanced tumor-targeting efficacy. These unique advantages of IVTPO greatly facilitate real-time optical imaging of GBM progression with high resolution and deep penetration depth through the intact skull (Fig. 6M).

DISCUSSION

Most commercial dyes fail to cross the BBB due to their large MW and unsuitable lipophilicity. We designed a series of hemicyanine dye molecules with a typical D-π-A architecture to maintain efficient optical properties of cyanine molecules. Through structural adjustment of the log *P* and MW of the probes, an amphiphilic hemicyanine probe (e.g., IVTPO) was obtained with effective BBB permeability. This probe inherits the characteristic advantages of cyanine with a high molar extinction coefficient and good biocompatibility and demonstrates unique merits different from cyanine dyes, e.g., good photostability and a negligible spectral overlap between absorption and emission. It exhibits outstanding BBB permeability.

Compared with the single imaging approach using FL imaging exclusively, the utilization of bimodal FL/photoacoustic imaging could remarkably improve imaging penetration depth even through the intact skull. Such merit enables maintenance of the native environment of the brain and an intact BBB, which greatly favors noninvasive acquisition of high-resolution images in deep tissues of the brain. Abnormal leakage of IVTPO adjacent to the developing tumor is unambiguously observed at an early stage of tumor advancement before the impairment of BBB integrity, as assessed by EB. Compared with commercial EB, IVTPO demonstrates enhanced optical imaging capability and improved tumor-targeting efficacy. It is noteworthy that optical imaging and the corresponding IVTPO probe enable effective monitoring of GBM progression using an in vivo and real-time approach, which is markedly distinct from the traditional pathologic analysis method. In addition, our experimental findings demonstrate a substantial increase in the

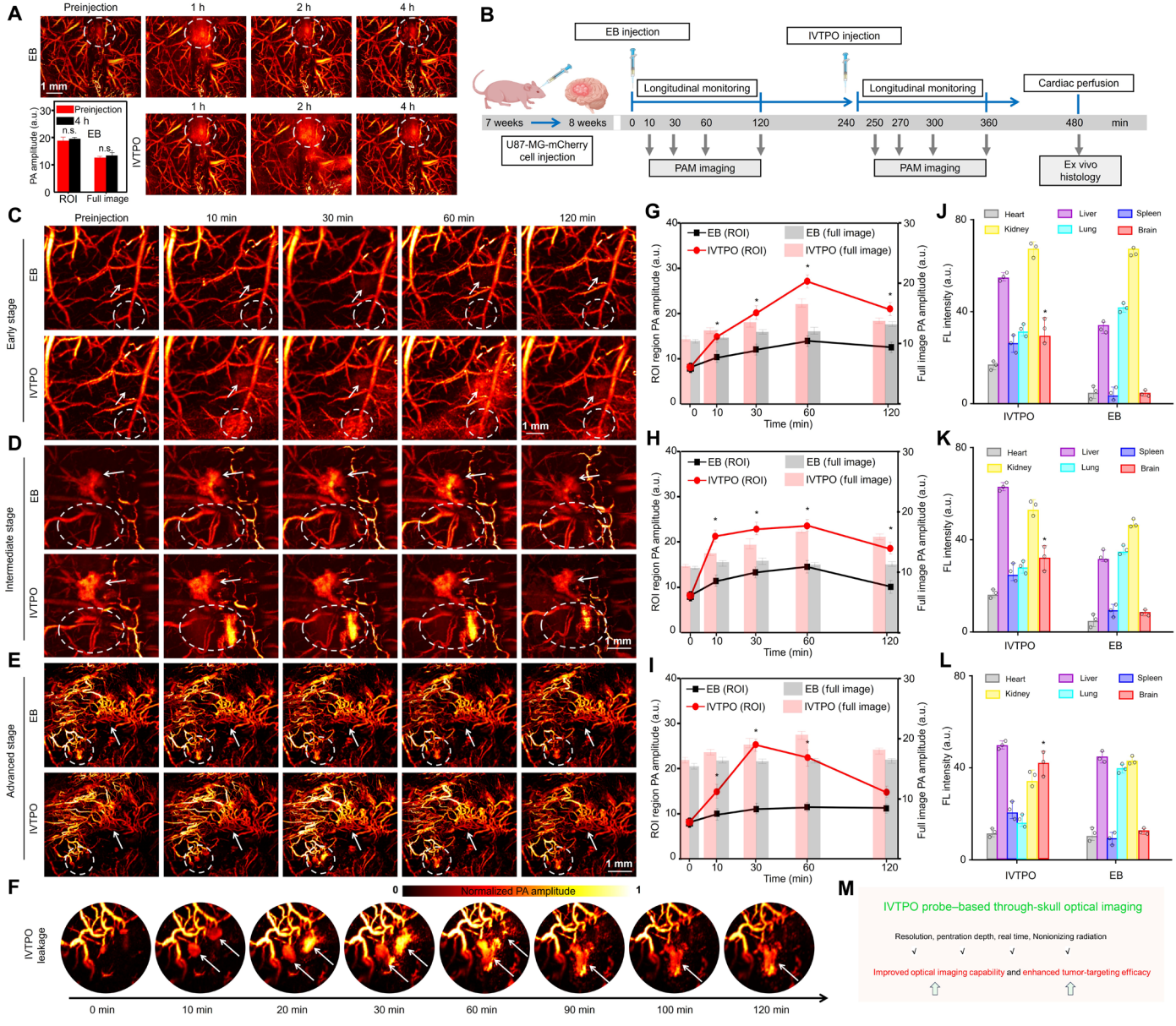

Fig. 6. In vivo photoacoustic imaging of GBM through the intact skull and biodistribution data. (**A**) Photoacoustic images and quantitative data of cerebral vessels of a GBM-bearing mouse after intravenous injection of EB and subsequent injection of IVTPO at various time points. (**B**) Schematic diagram of the timeline of experimental procedures during tumor progression in GBM-bearing mice. (**C** to **E**) Representative photoacoustic images of cerebral vessels of GBM-bearing mice in the (C) early stage, (D) intermediate stage, and (E) advanced stage before and after intravenous injection of EB or IVTPO at different time points (10 to 120 min). (**F**) Enlarged photoacoustic images of cerebral vessels of the GBM-bearing mouse in the advanced stage of GBM before and after intravenous injection of IVTPO at different time points (10 to 120 min). (**G** to **I**) Quantitative results of the ROI and full images of cerebral vessels of GBM-bearing mice in the (G) early, (H) intermediate, and (I) advanced stage. (**J** to **L**) Quantitative analysis of the ex vivo FL in major organs of GBM-bearing mice in the (J) early stage, (K) intermediate stage, and (L) advanced stage after the intravenous injection of IVTPO for 1 hour. (**M**) Advantages of through-skull optical imaging based on the IVTPO probe.

diameter of blood vessels within the tumor region following IVTPO injection, whereas the vessels in the peritumoral and normal regions exhibit no notable changes. This distinct characteristic offers valuable insights into enhancing tumor imaging. IVTPO may have additional biomedical applications, such as image-guided surgery, photodynamic therapy, and photothermal therapy. Exploration of these further applications is underway and will be realized in future research.

In summary, we have designed and facilely synthesized a series of optical probes with a characteristic D-π-A architecture. Our systematic study reveals that structural adjustment of log *P* and MW improves BBB permeability and optical properties of probes. IVTPO is chosen for optical bioimaging because of its high molar extinction coefficient (up to 12.29×10^4 M^{-1} cm^{-1}), good photostability, low cytotoxicity, and effective BBB penetrability. IVTPO is then applied as an efficient optical probe for in vivo imaging of intracranial GBM

with high resolution and deep penetration. The precise location of intracranial GBM, notable leakage of IVTPO from peritumoral blood vessels, and characteristic alterations in microvascular structure and BBB integrity at various stages of tumor advancement are readily identified. Even during the initial stage of tumor growth, anomalous leakage of IVTPO could be distinctly observed near the tumor location. This observation has important implications for the early detection and diagnosis of GBM. Compared with commercial EB dye, IVTPO exhibits enhanced optical imaging capability and improved tumor-targeting efficacy. Overall, our findings demonstrate the great promise of functional optical probes in noninvasive bimodal FL/photoacoustic imaging of intracranial GBM in vivo.

MATERIALS AND METHODS

Synthetic materials

2,3,3-Trimethylindolenine (**1**), 1,3-propanesultone (**2**), 4-(4-morpholinyl) benzaldehyde (**4a**), 5-morpholino-2-thiophenecarbaldehyde (**4b**), 5-(4-hydroxypiperidin-1-yl)thiophene-2-carbaldehyde (**4c**), 3-methylpiperidine, 1,4-dioxane, ethanol, petroleum ether (60° to 90°C), DCM, and methanol were purchased from Innochem and Energy Chemical in China. All the organic solvents and chemical regents were used as received without any further purification. Thin-layer chromatography was performed on GEL 60 F254 silica gel plates from Merck (Germany) and visualized by exposure to 254- and 365-nm ultraviolet (UV) irradiation. Column chromatography for the purification of organic compounds was carried out on 200 to 300 mesh Qingdao silica gel.

Chemical and optical characterization

^{1}H and ^{13}C NMR spectra were carried out on a Bruker AV 500 or 600 spectrometer in DMSO-d_6 or DCM-d_2. Chemical shifts are reported in parts per million, and coupling constants are given in hertz. Multiplicities are reported as s (singlet), d (doublet), t (triplet), q (quartet), m (multiplet), dd (doublet of doublet), etc. The high-resolution mass spectra were measured on an Orbitrap Fusion Lumos Tribrid mass spectrometer with an atmospheric pressure chemical ionization (APCI) source. The ultraperformance liquid chromatography–mass spectrometry analysis was performed in a Dionex UltiMate 3000 System (Thermo Fisher Scientific) coupled to an Orbitrap Fusion Lumos mass spectrometer (Thermo Fisher Scientific). UV-visible (UV-vis) absorption spectra were taken on a PerkinElmer Lambda 950 spectrophotometer. An FLS980 fluorescence spectrometer (Edinburgh Instruments) was used to test the photoluminescence spectra of probes.

Synthesis of probes

Preparation of 2,3,3-trimethyl-1-(propan-3-sulfonyl)indolenine (**3**): 2,3,3-Trimethylindolenine (**1**) (6.36 g, 40 mmol), 1,3-propanesultone (**2**) (5.12 g, 42 mmol), and dry 1,4-dioxane (60 ml) was heated at 90°C for 20 hours under nitrogen. Afterward, the mixture was cooled to room temperature and the resulting precipitate was collected by filtration. After washing with ethyl acetate (30 ml) and hexane (30 ml), the product was afforded as a light pink solid in 66.1% yield (7.44 g). ^{1}H NMR (600 MHz, DMSO-d_6) δ 8.05 (dd, J = 6.9, 1.9 Hz, 1H), 7.83–7.81 (m, 1H), 7.62 (tt, J = 7.4, 6.0 Hz, 2H), 4.67–4.65 (m, 2H), 2.83 (s, 3H), 2.62 (t, J = 6.5 Hz, 2H), 2.18–2.14 (m, 2H), and 1.53 (s, 6H). ^{13}C NMR (151 MHz, DMSO-d_6) δ 196.52, 141.92, 141.18, 129.30, 128.92, 123.39, 115.44, 54.09, 47.34, 46.57, 23.72, 22.02, and 13.75. Fourier transform mass spectrometry (FTMS) (using APCI source) mass/charge ratio (m/z): $[M + H]^+$ calcd for $C_{14}H_{20}NO_3S^+$, 282.1159; found, 282.1157.

Preparation of IVPM (**5a**): A mixture of 2,3,3-trimethyl-1-(propan-3-sulfonyl)indolenine (**3**) (562 mg, 2 mmol), 4-(4-morpholinyl) benzaldehyde (**4a**) (478 mg, 2.5 mmol), 3-methylpiperidine (0.5 ml), and anhydrous ethanol (20 ml) was stirred at room temperature for 48 hours. After solvent evaporation under reduced pressure, the final product was purified by silica gel column chromatography using DCM/methanol as the eluent. IVPM was obtained as a solid powder (556 mg) in 61.2% yield. ^{1}H NMR (500 MHz, DMSO-d_6) δ 8.35 (d, J = 15.7 Hz, 1H), 8.19 (d, J = 8.7 Hz, 2H), 7.86 (d, J = 7.9 Hz, 1H), 7.79 (d, J = 7.3 Hz, 1H), 7.60 (d, J = 15.7 Hz, 1H), 7.56 (t, J = 7.3 Hz, 1H), 7.50 (t, J = 7.4 Hz, 1H), 7.08 (d, J = 8.8 Hz, 2H), 4.73 (t, J = 7.9 Hz, 2H), 3.74 (t, J = 4.9 Hz, 4H), 3.50 (t, J = 4.9 Hz, 4H), 2.65 (t, J = 6.3 Hz, 2H), 2.16–2.10 (m, 2H), and 1.76 (s, 6H). ^{13}C NMR (126 MHz, DMSO-d_6) δ 180.13, 154.56, 154.53, 143.01, 141.04, 134.17, 128.86, 127.90, 124.22, 122.82, 113.97, 113.38, 106.74, 65.79, 51.17, 47.29, 46.36, 44.46, 26.27, and 24.29. FTMS (APCI source) m/z: $[M + H]^+$ calcd for $C_{25}H_{31}N_2O_4S^+$,455.2000; found, 455.1997.

Preparation of IVTM (**5b**): The compound was prepared from 2,3,3-trimethyl-1-(propan-3-sulfonyl)indolenine (**3**) (422 mg, 1.5 mmol), 5-morpholino-2-thiophenecarbaldehyde (**4b**) (433 mg, 2.2 mmol), 3-methylpiperidine (0.5 ml), and anhydrous ethanol (20 ml), following the same procedure described above. Yield: 60.6% (418 mg). ^{1}H NMR (600 MHz, DCM-d_2) δ 8.16 (d, J = 14.3 Hz, 1H), 7.70 (s, 1H), 7.44 (t, J = 7.7 Hz, 1H), 7.40 (d, J = 6.9 Hz, 1H), 7.31 (t, J = 7.2 Hz, 2H), 6.62 (d, J = 14.3 Hz, 1H), 6.42 (d, J = 4.9 Hz, 1H), 4.51–4.49 (m, 2H), 3.88–3.86 (m, 4H), 3.65–3.57 (m, 4H), 2.90–2.88 (m, 2H), 2.28–2.24 (m, 2H), and 1.67 (s, 6H). ^{13}C NMR (151 MHz, DCM-d_2) δ 175.63, 173.63, 147.27, 144.86, 142.24, 141.45, 129.32, 127.53, 126.37, 122.61, 111.92, 110.14, 100.56, 66.16, 50.86, 50.25, 47.73, 44.51, 27.86, and 23.97. FTMS (APCI source) m/z: $[M + H]^+$ calcd for $C_{23}H_{29}N_2O_4S_2^+$, 461.1564; found, 461.1561.

Preparation of IVTPO (**5c**): The compound was prepared from 2,3,3-trimethyl-1-(propan-3-sulfonyl)indolenine (**3**) (562 mg, 2.0 mmol), 5-(4-hydroxypiperidin-1-yl)thiophene-2-carbaldehyde (**4c**) (528 mg, 2.5 mmol), 3-methylpiperidine (0.5 ml), and anhydrous ethanol (20 ml), following the same procedure described above and using DCM to wash the product. Yield: 80.2% (760 mg). ^{1}H NMR (600 MHz, DMSO-d_6) δ 8.38 (d, J = 14.2 Hz, 1H), 8.03 (s, 1H), 7.60 (d, J = 7.4 Hz, 1H), 7.51 (d, J = 8.0 Hz, 1H), 7.41 (t, J = 7.7 Hz, 1H), 7.26 (t, J = 7.4 Hz, 1H), 6.86 (s, 1H), 6.23 (d, J = 14.1 Hz, 1H), 4.96 (d, J = 3.9 Hz, 1H), 4.33 (s, 2H), 3.89–3.85 (m, 3H), 3.60–3.58 (m, 2H), 2.55 (t, J = 6.9 Hz, 2H), 2.01 (p, J = 7.1 Hz, 2H), 1.92 (ddt, J = 13.8, 7.2, 3.6 Hz, 2H), 1.66 (s, 6H), and 1.59 (dp, J = 12.5, 4.0 Hz, 2H). ^{13}C NMR (151 MHz, DMSO-d_6) δ 173.63, 172.59, 148.90, 143.28, 141.91, 140.93, 128.44, 126.04, 124.95, 122.34, 111.79, 111.41, 97.75, 63.70, 54.86, 49.13, 48.77, 47.81, 42.74, 33.22, 26.96, and 23.40. FTMS (APCI source) m/z: $[M + H]^+$ calcd for $C_{24}H_{31}N_2O_4S_2^+$, 475.1720; found, 475.1719.

Theoretical calculations

Theoretical calculations were performed using the Gaussian 09 software. Vertical ionization energies of probes were optimized at the ωB97XD/Def2-SVP level. Molecular geometries of probes in the ground state were optimized at the B3LYP/6-31G(d) level.

Measurement of the oil-water partition coefficient

The oil-water partition coefficient (log *P*) was determined by a shake flask method. First, *n*-octanol and water were shaken in a shaker for 24 hours, and then the solution was placed in a centrifuge (5000 rpm) for 0.5 hours to separate the two phases. The upper layer was the oil phase (*n*-octanol saturated with water), and the lower layer was the water phase saturated with octanol. A dye was dissolved in *n*-octanol phase, which was presaturated with water. The dye in *n*-octanol phase was mixed with an equal volume of water phase saturated with octanol. Then, the mixture was placed in a regular shaker at room temperature for 24 hours, followed by in a centrifuge (5000 rpm) for 0.5 hours to separate the two phases. The concentration of probe was measured by UV-vis spectroscopy, and the log *P* value was calculated by the following formula: $\log P = \log ([\text{dye}]_{\text{oil phase}}/[\text{dye}]_{\text{water phase}})$ (*63*).

In vitro and in vivo experiments

Cell targeting in vitro: The macrophage cells and U87-MG cell lines were selected to assess the probe's cellular targeting efficacy. IVTPO was coincubated with 5×10^4 cells for 1 hour at a concentration of 50 μg/ml. Laser scanning confocal microscopy (FV1200, Olympus, Tokyo, Japan) was used to quantitatively evaluate the targeting characteristics of the probe.

In vitro cell viability test: Cell viability was measured by acetoxymethyl ester/propidium iodide (AM/PI) assays (Dojindo Molecular Technologies Inc., USA). U87-MG and macrophage cells (1×10^4) were cultured on 96-well plates and incubated at room temperature for 24 hours. Furthermore, they were incubated with IVTPO (10 to 100 μg/ml) for 24 hours and then washed twice with PBS. In addition, 2×10^6 U87-MG cells were cultured in 100 PI cell culture dishes for 36 hours. Cells were trypsinized and resuspended in 500 μl of RPMI 1640 medium with 10% fetal bovine serum (FBS) (Thermo Fisher Scientific Inc., USA). Then, calcium fluorescein AM and PI (Abcam plc., USA) were applied to stain the living and dead cells, and the cell images were recorded by a laser confocal FL microscope (FV1200, Olympus, Tokyo, Japan).

Animal preparation: Balb/c nude mice (6 weeks old, with equal numbers of males and females, sourced from the Guangdong Medical Laboratory Animal Center) were housed in accordance with standard guidelines. They were provided with ad libitum access to food and water and maintained under a 12-hour/12-hour light/dark cycle. The environmental conditions, including temperature (24° to 26°C) and humidity (50 to 70%), were consistently regulated throughout the study. Mouse cages underwent regular high-temperature sterilization, and corncob bedding was routinely replaced to maintain a sterile and dry environment. Following a 1-week acclimation period, all mice were randomly assigned to experimental groups.

Orthotopic xenografting GBM model preparation: The U87-MG human GBM multiforme cell line was obtained from the American Type Culture Collection and maintained in Dulbecco's modified Eagle's medium (Gibco, 21063-029) supplemented with 10% FBS (Gibco, 10270-106), and 1% antibiotic-antimycotic solution at 37°C in a 5% CO_2 atmosphere. Balb/c nude mice (6 weeks old, obtained from the Guangdong Medical Laboratory Animal Center) were housed according to standard guidelines, with ad libitum access to food and water, under a 12-hour/12-hour light/dark cycle. Mice were monitored daily for signs of tumor development. The age classifications were as follows: early stage (7 to 9 weeks), intermediate stage (9 to 11 weeks), and advanced stage (11 to 13 weeks). Mice were anesthetized and maintained using 1.5% vaporized isoflurane. Following aseptic procedures to expose the skull, the skull was immobilized, and 10 μl of U87-MG cells (10^6 cells/ml) were stereotactically implanted into the mouse brain using a digital pump at an infusion rate of 1 μl/min with a Hamilton syringe. After infusion, the syringe needle was incrementally raised by 0.5 mm and maintained in position for at least 3 min to improve infiltration and minimize backflow of the injected cell suspension. Subsequently, a tiny opening was left in the skull, which naturally closed within 5 to 7 days after injection, restoring the skull to its intact state. Mice were monitored daily for signs of tumor development. All animal experiments were performed in compliance with the Guidelines for the Care and Use of Research Animals established by the Institutional Ethical Committee of Animal Experimentation of Guangdong Provincial People's Hospital (KY2024-095-01) in China.

In vivo imaging of the orthotopic GBM model: In this study, a high-resolution PAM system (Inno Laser Technology Co. Ltd.) was used for in vivo imaging of cerebral vessels in an orthotopic GBM model. In the context of cerebrovascular imaging, the photoacoustic transducer was immersed in a tank containing deionized water. After securing the head in place using a specially designed holder, an incision was made along the midline of the scalp to create a wound measuring ~2 cm in length. Imaging procedures were carried out with the skull remaining undisturbed. Hemostasis was achieved using a hemostatic sponge, followed by the application of sterile ultrasound gel to preserve skull moisture and reduce signal loss during signal propagation. In the experiment examining dye accumulation within the tumor, the concentrations of EB and IVTPO were set at 50 μg/ml, with an injection volume of 200 μl. However, in the experiment designed to investigate tumor progression, an aqueous solution of EB (20 μg/ml, 80 μl) was administered via the tail vein of the mice. Four hours after the initial injection, an aqueous solution of IVTPO (20 μg/ml, 80 μl) was also administered via the tail vein of the mice.

Photoacoustic imaging data acquisition: The system operated at a laser repetition rate of 5 kHz with a pulse width of 7 ns. Each pulse delivered laser energy set at 800 nJ per pulse. Scanning was conducted over areas of 1 mm^2 (with a step size of 3 μm), 2 mm^2 (step size of 3 μm), 3 mm^2 (step size of 3 μm), 5 mm^2 (step size of 5 μm), and 10 mm^2 (step size of 10 μm). The acoustic signal, generated from laser irradiation on the imaging tissue, was captured by a 50-MHz ultrasonic sensor and then amplified by a 50-dB amplifier. Photoacoustic images were subsequently acquired and reconstructed from the datasets using MATLAB (MathWorks, USA) sequentially.

Biodistribution study: To investigate the biodistribution of IVTPO, mice were anesthetized via intraperitoneal injection of 1% sodium pentobarbital at 50 mg/kg. After cardiac perfusion with ~20 ml of normal saline, brain tissue and organs were harvested. The tissues were weighed, immersed in a threefold volume of normal saline, and homogenized. The resulting homogenized solution was then centrifuged at 10,000 rpm at 4°C for 10 min, and the supernatant obtained was used for analysis. The biodistribution of IVTPO in the major organs and brains of tumor-bearing mice was systematically examined using an FL imaging system (IVIS Spectrum, PerkinElmer) at 4 hours after injection.

Statistical analysis: Quantitative data were expressed as means ± SD and were analyzed using the GraphPad Prism 7.0 software. The paired *t* test was used to assess the statistical significance of differences in extracted vascular parameters across different tumor stages within each group. Statistical significance was denoted as $*P < 0.05$ and $**P < 0.01$. A *P* value below 0.05 was considered statistically significant.

Supplementary Materials

The PDF file includes:
Figs. S1 to S18
Legend for movie S1

Other Supplementary Material for this manuscript includes the following:
Movie S1

REFERENCES ANE NOTES

1. M. Lim, Y. Xia, C. Bettegowda, M. Weller, Current state of immunotherapy for glioblastoma. *Nat. Rev. Clin. Oncol.* **15**, 422–442 (2018).
2. M. Yao, S. Li, X. Wu, S. Diao, G. Zhang, H. He, L. Bian, Y. Lu, Cellular origin of glioblastoma and its implication in precision therapy. *Cell. Mol. Immunol.* **15**, 737–739 (2018).
3. Q. T. Ostrom, H. Gittleman, P. Liao, T. Vecchione-Koval, Y. Wolinsky, C. Kruchko, J. S. Barnholtz-Sloan, CBTRUS Statistical Report: Primary brain and other central nervous system tumors diagnosed in the United States in 2010–2014. *Neuro. Oncol.* **19**, v1–v88 (2017).
4. W. Wu, J. L. Klockow, M. Zhang, F. Lafortune, E. Chang, L. Jin, Y. Wu, H. E. Daldrup-Link, Glioblastoma multiforme (GBM): An overview of current therapies and mechanisms of resistance. *Pharmacol. Res.* **171**, 105780 (2021).
5. P. Y. Wen, D. A. Reardon, Progress in glioma diagnosis, classification and treatment. *Nat. Rev. Neurol.* **12**, 69–70 (2016).
6. J. Miao, M. Miao, Y. Jiang, M. Zhao, Q. Li, Y. Zhang, Y. An, K. Pu, Q. Miao, An activatable NIR-II fluorescent reporter for in vivo imaging of amyloid-β plaques. *Angew. Chem. Int. Ed. Engl.* **62**, e202216351 (2023).
7. Y. Chen, S. Wang, F. Zhang, Near-infrared luminescence high-contrast in vivo biomedical imaging. *Nat. Rev. Bioeng.* **1**, 60–78 (2023).
8. M. M. Kim, A. Parolia, M. P. Dunphy, S. Venneti, Non-invasive metabolic imaging of brain tumours in the era of precision medicine. *Nat. Rev. Clin. Oncol.* **13**, 725–739 (2016).
9. G. Hong, A. L. Antaris, H. Dai, Near-infrared fluorophores for biomedical imaging. *Nat. Biomed. Eng.* **1**, 0010 (2017).
10. S. Samanta, K. Lai, F. Wu, Y. Liu, S. Cai, X. Yang, J. Qu, Z. Yang, Xanthene, cyanine, oxazine and BODIPY: The four pillars of the fluorophore empire for super-resolution bioimaging. *Chem. Soc. Rev.* **52**, 7197–7261 (2023).
11. S. Zeng, X. Liu, Y. S. Kafuti, H. Kim, J. Wang, X. Peng, H. Li, J. Yoon, Fluorescent dyes based on rhodamine derivatives for bioimaging and therapeutics: Recent progress, challenges, and prospects. *Chem. Soc. Rev.* **52**, 5607–5651 (2023).
12. X. L. Deán-Ben, S. Gottschalk, B. McLarney, S. Shoham, D. Razansky, Advanced optoacoustic methods for multiscale imaging of in vivo dynamics. *Chem. Soc. Rev.* **46**, 2158–2198 (2017).
13. Z. Hu, C. Fang, B. Li, Z. Zhang, C. Cao, M. Cai, S. Su, X. Sun, X. Shi, C. Li, T. Zhou, Y. Zhang, C. Chi, P. He, X. Xia, Y. Chen, S. S. Gambhir, Z. Cheng, J. Tian, First-in-human liver-tumour surgery guided by multispectral fluorescence imaging in the visible and near-infrared-I/II windows. *Nat. Biomed. Eng.* **4**, 259–271 (2020).
14. H. Chen, L. Liu, K. Qian, H. Liu, Z. Wang, F. Gao, C. Qu, W. Dai, D. Lin, K. Chen, H. Liu, Z. Cheng, Bioinspired large Stokes shift small molecular dyes for biomedical fluorescence imaging. *Sci. Adv.* **8**, eabo3289 (2022).
15. B. Li, H. Xiao, M. Cai, X. Li, X. Xu, S. Wang, S. Huang, Y. Wang, D. Cheng, P. Pang, H. Shan, X. Shuai, Molecular probe crossing blood–brain barrier for bimodal imaging–guided photothermal/photodynamic therapies of intracranial glioblastoma. *Adv. Funct. Mater.* **30**, 1909117 (2020).
16. A. P. McMahon, J. K. Ichida, Repairing the blood-brain barrier. *Science* **375**, 715–716 (2022).
17. M. Martin, S. Vermeiren, N. Bostaille, M. Eubelen, D. Spitzer, M. Vermeersch, C. P. Profaci, E. Pozuelo, X. Toussay, J. Raman-Nair, P. Tebabi, M. America, A. De Groote, L. E. Sanderson, P. Cabochette, R. F. V. Germano, D. Torres, S. Boutry, A. de Kerchove d'Exaerde, E. J. Bellefroid, T. N. Phoenix, K. Devraj, B. Lacoste, R. Daneman, S. Liebner, B. Vanhollebeke, Engineered Wnt ligands enable blood-brain barrier repair in neurological disorders. *Science* **375**, eabm4459 (2022).
18. D. Wu, Q. Chen, X. Chen, F. Han, Z. Chen, Y. Wang, The blood–brain barrier: Structure, regulation, and drug delivery. *Signal Transduct. Target. Ther.* **8**, 217 (2023).
19. M. Malakoutikhah, M. Teixidó, E. Giralt, Shuttle-mediated drug delivery to the brain. *Angew. Chem. Int. Ed.* **50**, 7998–8014 (2011).
20. Y.-B. Miao, K.-H. Chen, C.-T. Chen, F.-L. Mi, Y.-J. Lin, Y. Chang, C.-S. Chiang, J.-T. Wang, K.-J. Lin, H.-W. Sung, A noninvasive gut-to-brain oral drug delivery system for treating brain tumors. *Adv. Mater.* **33**, 2100701 (2021).
21. G. C. Terstappen, A. H. Meyer, R. D. Bell, W. Zhang, Strategies for delivering therapeutics across the blood–brain barrier. *Nat. Rev. Drug Discov.* **20**, 362–383 (2021).
22. S. Zha, H. Liu, H. Li, H. Li, K.-L. Wong, A. H. All, Functionalized nanomaterials capable of crossing the blood–brain barrier. *ACS Nano* **18**, 1820–1845 (2024).
23. Y. Wang, X. Wang, R. Xie, J. C. Burger, Y. Tong, S. Gong, Overcoming the blood–brain barrier for gene therapy via systemic administration of GSH-responsive silica nanocapsules. *Adv. Mater.* **35**, 2208018 (2023).
24. Y. Zou, Y. Wang, S. Xu, Y. Liu, J. Yin, D. B. Lovejoy, M. Zheng, X.-J. Liang, J. B. Park, Y. M. Efremov, I. Ulasov, B. Shi, Brain co-delivery of temozolomide and cisplatin for combinatorial glioblastoma chemotherapy. *Adv. Mater.* **34**, 2203958 (2022).
25. D. Furtado, M. Björnmalm, S. Ayton, A. I. Bush, K. Kempe, F. Caruso, Overcoming the blood–brain barrier: The role of nanomaterials in treating neurological diseases. *Adv. Mater.* **30**, 1801362 (2018).
26. H.-Y. Huang, H.-L. Liu, P.-H. Hsu, C.-S. Chiang, C.-H. Tsai, H.-S. Chi, S.-Y. Chen, Y.-Y. Chen, A multitheragnostic nanobubble system to induce blood–brain barrier disruption with magnetically guided focused ultrasound. *Adv. Mater.* **27**, 655–661 (2015).
27. J. Chen, J. Pan, S. Liu, Y. Zhang, S. Sha, H. Guo, X. Wang, X. Hao, H. Zhou, S. Tao, Y. Wang, J.-B. Fan, Fruit-derived extracellular-vesicle-engineered structural droplet drugs for enhanced glioblastoma chemotherapy. *Adv. Mater.* **35**, 2304187 (2023).
28. S. Wang, H. Shi, L. Wang, A. Loredo, S. M. Bachilo, W. Wu, Z. Tian, Y. Chen, R. B. Weisman, X. Zhang, Z. Cheng, H. Xiao, Photostable small-molecule NIR-II fluorescent scaffolds that cross the blood–brain barrier for noninvasive brain imaging. *J. Am. Chem. Soc.* **144**, 23668–23676 (2022).
29. M. Cui, M. Ono, H. Watanabe, H. Kimura, B. Liu, H. Saji, Smart near-infrared fluorescence probes with donor–acceptor structure for in vivo detection of β-amyloid deposits. *J. Am. Chem. Soc.* **136**, 3388–3394 (2014).
30. D. R. Groothuis, F. J. Vriesendorp, B. Kupfer, P. C. Warnke, G. D. Lapin, A. Kuruvilla, N. A. Vick, M. A. Mikhael, C. S. Patlak, Quantitative measurements of capillary transport in human brain tumors by computed tomography. *Ann. Neurol.* **30**, 581–588 (1991).
31. C. D. Arvanitis, G. B. Ferraro, R. K. Jain, The blood–brain barrier and blood–tumour barrier in brain tumours and metastases. *Nat. Rev. Cancer* **20**, 26–41 (2020).
32. W. Qin, N. Alifu, J. W. Y. Lam, Y. Cui, H. Su, G. Liang, J. Qian, B. Z. Tang, Facile synthesis of efficient luminogens with AIE features for three-photon fluorescence imaging of the brain through the intact skull. *Adv. Mater.* **32**, 2000364 (2020).
33. H. Su, T. Xie, Y. U. Liu, Y. Cui, W. Wen, B. Z. Tang, W. Qin, Facile synthesis of ultrabright luminogens with specific lipid droplets targeting feature for in vivo two-photon fluorescence retina imaging. *Chin. Chem. Lett.* **34**, 107949 (2023).
34. G. Yang, F. Pan, C. N. Parkhurst, J. Grutzendler, W.-B. Gan, Thinned-skull cranial window technique for long-term imaging of the cortex in live mice. *Nat. Protoc.* **5**, 201–208 (2010).
35. X. Wang, P. Li, Q. Ding, C. Wu, W. Zhang, B. Tang, Observation of acetylcholinesterase in stress-induced depression phenotypes by two-photon fluorescence imaging in the mouse brain. *J. Am. Chem. Soc.* **141**, 2061–2068 (2019).
36. H.-T. Xu, F. Pan, G. Yang, W.-B. Gan, Choice of cranial window type for in vivo imaging affects dendritic spine turnover in the cortex. *Nat. Neurosci.* **10**, 549–551 (2007).
37. Y. Chen, S. Liu, H. Liu, S. Tong, H. Tang, C. Zhang, S. Yan, H. Li, G. Yang, D. Zhu, K. Wang, P. Wang, Coherent Raman scattering unravelling mechanisms underlying skull optical clearing for through-skull brain imaging. *Anal. Chem.* **91**, 9371–9375 (2019).
38. L. Lin, L. V. Wang, The emerging role of photoacoustic imaging in clinical oncology. *Nat. Rev. Clin. Oncol.* **19**, 365–384 (2022).
39. X. Zhu, Q. Huang, L. Jiang, V.-T. Nguyen, T. Vu, G. Devlin, J. Shaima, X. Wang, Y. Chen, L. Ma, K. Xiang, E. Wang, Q. Rong, Q. Zhou, Y. Kang, A. Asokan, L. Feng, S.-W. D. Hsu, X. Shen, J. Yao, Longitudinal intravital imaging of mouse placenta. *Sci. Adv.* **10**, eadk1278 (2024).
40. X. Liu, Y. Duan, B. Liu, Nanoparticles as contrast agents for photoacoustic brain imaging. *Aggregate* **2**, 4–19 (2021).
41. K. Yang, B. Yu, W. Liu, Z. Zhang, L. Huang, S. Zhao, B. Wang, J. Yi, J. Yuan, Y. Zou, C. Lin, X. Song, M. Lan, All-in-one phototheranostics based on BTP-4F-DMO nanoparticles for NIR-II fluorescence/photoacoustic dual-mode imaging and combinational therapy. *Chin. Chem. Lett.* **34**, 107889 (2023).
42. J. Zhang, X. Yin, C. Li, X. Yin, Q. Xue, L. Ding, J. Ju, J. Ma, Y. Zhu, D. Du, R. L. Reis, Y. Wang, A multifunctional photoacoustic/fluorescence dual-mode-imaging gold-based theranostic nanoformulation without external laser limitations. *Adv. Mater.* **34**, 2110690 (2022).
43. D. Yan, T. Li, Y. Yang, N. Niu, D. Wang, J. Ge, L. Wang, R. Zhang, D. Wang, B. Z. Tang, A water-soluble AIEgen for noninvasive diagnosis of kidney fibrosis via SWIR fluorescence and photoacoustic imaging. *Adv. Mater.* **34**, 2206643 (2022).
44. M. Liang, L. Liu, Y. Sun, J. Li, L. Zhang, X. Jiang, W. Wu, Furan-modified thiadiazolo quinoxaline as an electron acceptor for constructing second near-infrared aggregation-

induced emission fluorophores for beyond 1300 nm fluorescence/photoacoustic imaging and photothermal therapy. *Aggregate* **5**, e458 (2024).
45. H. Shen, Y. Li, Y. Li, Self-assembly and tunable optical properties of intramolecular charge transfer molecules. *Aggregate* **1**, 57–68 (2020).
46. Z. Zeng, S. S. Liew, X. Wei, K. Pu, Hemicyanine-based near-infrared activatable probes for imaging and diagnosis of diseases. *Angew. Chem. Int. Ed. Engl.* **60**, 26454–26475 (2021).
47. X. Hu, C. Zhu, F. Sun, Z. Chen, J. Zou, X. Chen, Z. Yang, J-aggregation strategy toward potentiated NIR-II fluorescence bioimaging of molecular fluorophores. *Adv. Mater.* **36**, 2304848 (2024).
48. W. Liu, S. Deng, L. Zhang, C.-W. Ju, Y. Xie, W. Deng, J. Chen, H. Wu, Y. Cao, Short-wavelength infrared organic light-emitting diodes from A–D–A′–D–A type small molecules with emission beyond 1100 nm. *Adv. Mater.* **35**, 2302924 (2023).
49. Y. Fan, F. Wang, F. Hou, L. Wei, G. Zhu, D. Zhao, Q. Hu, T. Lei, L. Yang, P. Wang, G. Ge, A novel TICT-based near-infrared fluorescent probe for light-up sensing and imaging of human serum albumin in real samples. *Chin. Chem. Lett.* **34**, 107557 (2023).
50. W. Qin, D. Ding, J. Liu, W. Z. Yuan, Y. Hu, B. Liu, B. Z. Tang, Biocompatible nanoparticles with aggregation-induced emission characteristics as far-red/near-infrared fluorescent bioprobes for in vitro and in vivo imaging applications. *Adv. Funct. Mater.* **22**, 771–779 (2012).
51. W. Zhu, M. Kang, Q. Wu, Z. Zhang, Y. Wu, C. Li, K. Li, L. Wang, D. Wang, B. Z. Tang, Zwitterionic AIEgens: Rational molecular design for NIR-II fluorescence imaging-guided synergistic phototherapy. *Adv. Funct. Mater.* **31**, 2007026 (2021).
52. Z. Zhang, W. Xu, M. Kang, H. Wen, H. Guo, P. Zhang, L. Xi, K. Li, L. Wang, D. Wang, B. Z. Tang, An all-round athlete on the track of phototheranostics: Subtly regulating the balance between radiative and nonradiative decays for multimodal imaging-guided synergistic therapy. *Adv. Mater.* **32**, 2003210 (2020).
53. W. Xu, Z. Zhang, M. Kang, H. Guo, Y. Li, H. Wen, M. M. S. Lee, Z. Wang, R. T. K. Kwok, J. W. Y. Lam, K. Li, L. Xi, S. Chen, D. Wang, B. Z. Tang, Making the best use of excited-state energy: Multimodality theranostic systems based on second near-infrared (NIR-II) aggregation-induced emission luminogens (AIEgens). *ACS Mater. Lett.* **2**, 1033–1040 (2020).
54. D. Wang, M. M. S. Lee, G. Shan, R. T. K. Kwok, J. W. Y. Lam, H. Su, Y. Cai, B. Z. Tang, Highly efficient photosensitizers with far-red/near-infrared aggregation-induced emission for in vitro and in vivo cancer theranostics. *Adv. Mater.* **30**, 1802105 (2018).
55. W. Lin, L. Yuan, Z. Cao, Y. Feng, J. Song, Through-bond energy transfer cassettes with minimal spectral overlap between the donor emission and acceptor absorption: Coumarin–rhodamine dyads with large pseudo-stokes shifts and emission shifts. *Angew. Chem. Int. Ed. Engl.* **49**, 375–379 (2010).
56. W. Fu, C. Yan, Z. Guo, J. Zhang, H. Zhang, H. Tian, W.-H. Zhu, Rational design of near-infrared aggregation-induced-emission-active probes: In situ mapping of amyloid-β plaques with ultrasensitivity and high-fidelity. *J. Am. Chem. Soc.* **141**, 3171–3177 (2019).
57. M. Hintersteiner, A. Enz, P. Frey, A.-L. Jaton, W. Kinzy, R. Kneuer, U. Neumann, M. Rudin, M. Staufenbiel, M. Stoeckli, K.-H. Wiederhold, H.-U. Gremlich, In vivo detection of amyloid-β deposits by near-infrared imaging using an oxazine-derivative probe. *Nat. Biotechnol.* **23**, 577–583 (2005).
58. J. Xue, Z. Zhao, L. Zhang, L. Xue, S. Shen, Y. Wen, Z. Wei, L. Wang, L. Kong, H. Sun, Q. Ping, R. Mo, C. Zhang, Neutrophil-mediated anticancer drug delivery for suppression of postoperative malignant glioma recurrence. *Nat. Nanotechnol.* **12**, 692–700 (2017).
59. V. Balzer, P. Poc, E. Puris, S. Martin, M. Aliasgari, S. Auriola, G. Fricker, Re-evaluation of the hCMEC/D3 based in vitro BBB model for ABC transporter studies. *Eur. J. Pharm. Biopharm.* **173**, 12–21 (2022).
60. S. K. Golombek, J.-N. May, B. Theek, L. Appold, N. Drude, F. Kiessling, T. Lammers, Tumor targeting via EPR: Strategies to enhance patient responses. *Adv. Drug Deliver. Rev.* **130**, 17–38 (2018).
61. X. Cai, A. Bandla, D. Mao, G. Feng, W. Qin, L.-D. Liao, N. Thakor, B. Z. Tang, B. Liu, Biocompatible red fluorescent organic nanoparticles with tunable size and aggregation-induced emission for evaluation of blood–brain barrier damage. *Adv. Mater.* **28**, 8760–8765 (2016).
62. J. Zhang, X. Sun, H. Li, H. Ma, F. Duan, Z. Wu, B. Zhu, R. Chen, L. Nie, In vivo characterization and analysis of glioblastoma at different stages using multiscale photoacoustic molecular imaging. *Photoacoustics* **30**, 100462 (2023).
63. Y. Wang, D. Mei, X. Zhang, D.-H. Qu, J. Mei, Visualizing Aβ deposits in live young AD model mice with a simple red/near-infrared-fluorescent AIEgen. *Sci. China Chem.* **65**, 339–352 (2022).

Acknowledgments
Funding: The financial support was partially received from the National Natural Science Foundation of China [21971265 (W.Q.), 82425029 (L.N.), 82372010 (L.N.), and 82402340 (H.L.)] and National Key R&D Program of China [2023YFF0715303 (L.N.)]. **Author contributions:** W.Q. and L.N. designed the research. W.Q. designed and synthesized the optical probes and conducted experiments for their chemical and optical characterization. H.L. and J.C. performed in vitro and in vivo optical imaging experiments. Y.Q. conducted data processing. W.Q., H.L., J.C., L.M., and L.N. wrote and revised the paper. All authors reviewed the manuscript. **Competing interests:** The authors declare that they have no competing interests. **Data and materials availability:** All data needed to evaluate the conclusions in the paper are present in the paper and/or the Supplementary Materials.

Submitted 22 May 2024
Accepted 13 December 2024
Published 15 January 2025
10.1126/sciadv.adq5816